npj | quantum information

Article

Published in partnership with The University of New South Wales

https://doi.org/10.1038/s41534-025-01016-x

Industrial 300 mm wafer processed spin qubits in natural silicon/silicon-germanium

Thomas Koch[1] ✉, Clement Godfrin[2], Viktor Adam[3], Julian Ferrero[1], Daniel Schroller[1], Noah Glaeser[1], Stefan Kubicek[2], Ruoyu Li[2], Roger Loo[2,4], Shana Massar[2], George Simion[2], Danny Wan[2], Kristiaan De Greve[2,5] & Wolfgang Wernsdorfer[1,3] ✉

The realisation of a universal quantum computer will require the operation of many thousands to millions of coherently coupled qubits. The possibility of using existing industrial semiconductor fabrication techniques and infrastructure for up-scaling and reproducibility makes silicon based spin qubits one of the most promising platforms to achieve this goal. The implementation of the up to now largest semiconductor based quantum processor was realised in a silicon/silicon-germanium heterostructure known for its low charge noise, long qubit coherence times and fast driving speeds, but the high structural complexity creates challenges for industrial implementations. Here we demonstrate quantum dots hosted in a natural Si/SiGe heterostructure fully fabricated by an industrial 300 mm semiconductor wafer process line from heterostructure growth to Co micromagnet monolithic integration. We report charge noise values below 2 μeV/$\sqrt{\text{Hz}}$, spin relaxation times exceeding 1 s, and coherence times T_2^* and T_2^H of 1 μs and 50 μs respectively, for quantum wells grown using natural silicon. Further, we achieve Rabi frequencies up to 5 MHz and single qubit gate fidelities above 99%. In addition to scalability, the high reproducibility of the 300 mm processes enables the deterministic study of qubit metric dependencies on process parameters, which is essential for optimising qubit quality.

A quantum computer capable of solving relevant problems requires a large amount of interconnected qubits paired with high-fidelity gate operations. Semiconductor based spin qubits are one of the most promising platforms in order to achieve this goal[1,2]. Single and two qubit gate fidelities exceeding the error correction threshold have been demonstrated[3–5]. High-fidelity operations at elevated temperatures increase the available cooling power drastically and ease the combination with classical control electronics[6–8]. Long range coupling can be implemented by superconducting resonators or electron shuttles[9–11]. The realisation of the up to date largest semiconductor based quantum processor consists of six qubits hosted in quantum dots formed in an isotopically purified ^{28}Si quantum well strained between silicon-germanium layers[12]. The Si/SiGe heterostructure aims to decouple the quantum well from the defective semiconductor oxide interface, which is known as the main contribution for charge noise inside the sample[13–15]. Paired with micromagnets that enable qubit manipulation by electric dipole spin resonance (EDSR), Rabi frequencies of several MHz and gate fidelities exceeding the error correction threshold were demonstrated[3]. Meanwhile, industrial CMOS fabrication technologies have advanced to the point where they can produce classical processors containing up to trillions of MOSFETs[16]. Utilising these fabrication techniques in the production of semiconducting qubits has the potential to enhance reproducibility and uniformity, as well as simplify the optimisation and fine-tuning of qubit parameters. These are all crucial steps towards the realisation of a universal quantum computer. Qubits fabricated with industrial semiconductor manufacturing technologies have been demonstrated recently for Si-MOS[17–19] and Si/SiGe heterostructures[20] and report quantum dot yields above 99%. However, the qubit control modules, specifically the micromagnets used for fast EDSR control, have not yet been fully integrated into the process flow. In this work, we demonstrate the operation of EDSR qubits in a natural Si/SiGe heterostructure, fully manufactured by an industrial

[1]Physikalisches Institut, Karlsruhe Institute of Technology (KIT), Karlsruhe, Germany. [2]Interuniversity Microelectronics Centre (imec), Leuven, Belgium. [3]Institute for Quantum Materials and Technologies, Karlsruhe Institute of Technology (KIT), Karlsruhe, Germany. [4]Department of Solid-State Sciences, Ghent University, Ghent, Belgium. [5]Department of Electrical Engineering, ESAT-MNS and Proximus Chair in Quantum Science and Technology, KU Leuven, Leuven, Belgium. ✉e-mail: T.Koch@kit.edu; Wolfgang.Wernsdorfer@kit.edu

300 mm semiconductor wafer process line, with a cobalt micromagnet control module incorporated through monolithic integration.

Results and discussion

Device fabrication and charge control

The natSi/SiGe heterostructures are grown on a 300 mm silicon wafer. From bottom to top, the heterostructure comprises a 8 µm strained relaxed buffer (SRB) finished by an unstrained 1 µm $Si_{0.75}Ge_{0.25}$ layer of constant concentration. This is followed by chemical vapour deposition (CVD) of a tensile-strained natSi quantum well of 9 nm and a $Si_{0.75}Ge_{0.25}$ buffer layer of 40 nm thickness. To avoid oxidation of the SiGe buffer, a 2 nm thick silicon cap is grown on top of the heterostructure. Ohmic contacts to the natSi quantum well are formed by phosphorus implants. Three overlapping gate layers made of titanium nitride (TiN) and insulated by silicon oxide (SiO_2) (From bottom to top: 8 nm SiO_2, 30 nm TiN, 5 nm SiO_2, 20 nm TiN, 5 nm SiO_2, 20 nm TiN) are used for the formation and manipulation of the quantum dots. More details regarding the gate-stack lithography can be found in ref. 21. A cobalt micromagnet (CoMM) module is made in line using a so-called Damascene process, as commonly used in back-end-of-line processing. A full sheet of oxide and photoresist is deposited across the 300 nm wafer. Next, the photoresist is patterned using deep ultraviolet (DUV) lithography. Following this, a gap is etched into the oxide using dry etching techniques. Subsequently, a full sheet of cobalt is deposited on the 300 nm wafer. Finally, the wafer undergoes chemical mechanical polishing (CMP) down to the oxide layer. A SiO_2 passivation layer is deposited on top of the whole stack. Vias are etched in this passivation layer to connect the ohmics, gate layers and the CoMM (see Fig. 1a). The gate layout of the device is shown in the false coloured scanning electron microscopy (SEM) picture in Fig. 1b. The architecture is designed to enable the formation of two quantum dots in the single electron regime, later used as qubits, and an adjacent single electron transistor (SET) for readout. The qubit dots are centred below the gap of a C-shaped CoMM, which creates an inhomogeneous external magnetic field at the qubit positions. By applying a microwave signal at the central screening gate (CC), the position of the qubit dot will oscillate, effectively creating an AC magnetic field with the frequency of the applied microwave signal[22]. Figure 1c shows the measured tunnel current through the right qubit quantum dot over varying voltages applied at the plunger gate PR. Coulomb oscillations of the measured current become visible. It was shown that the charge noise affecting a quantum dot can strongly differ for different working points[21]. In order to extract a value for

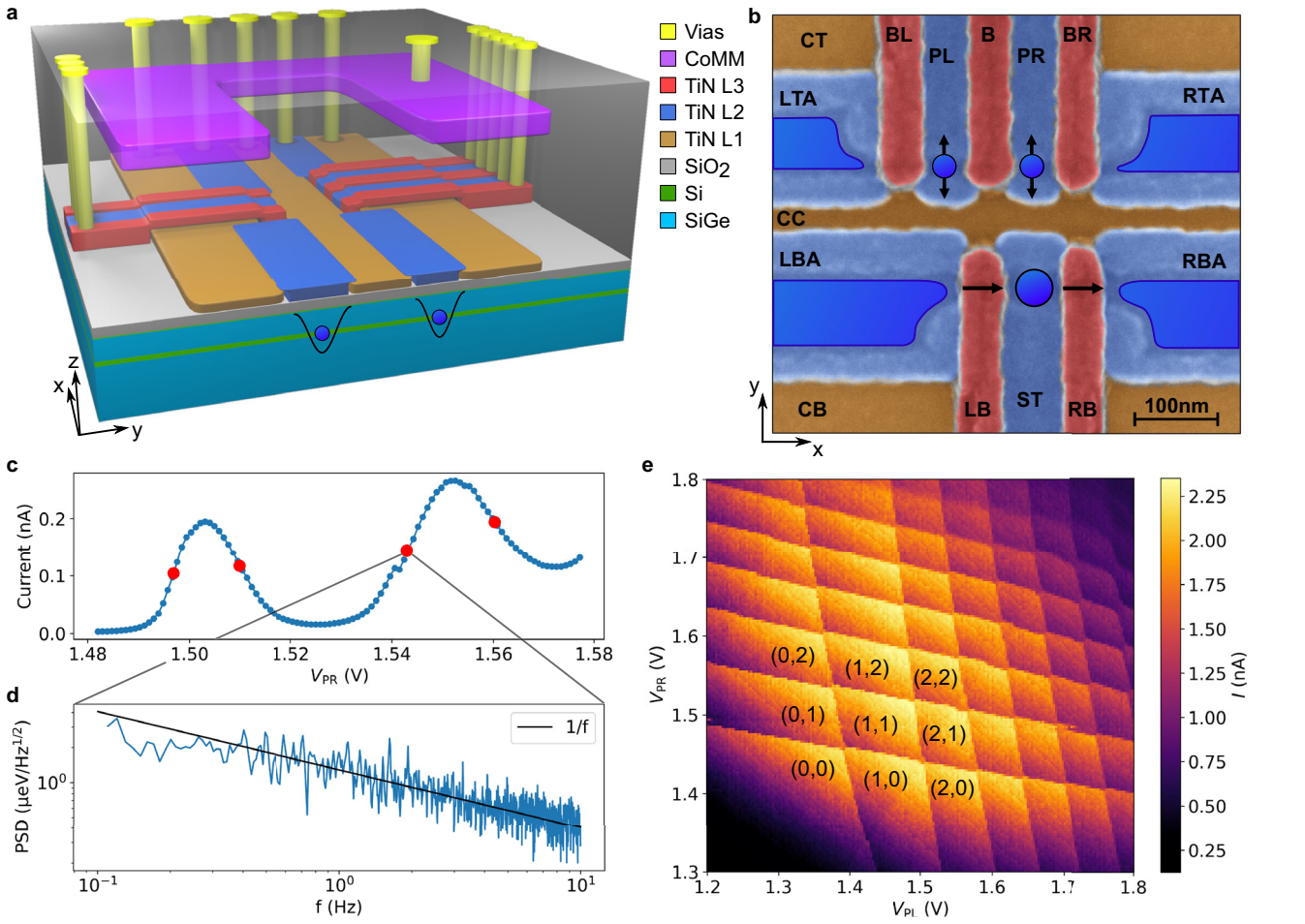

Fig. 1 | Device architecture and charge control. a 3D model of the device. 3-layer TiN gate architecture (orange, blue, red) on the SiGe heterostructure (cyan and green). SiO_2 (grey) insulates the different layers from each other. The electron gas is formed in the buried Si layer. The CoMM (violet) is encapsulated by a SiO_2 passivation layer, and all structures are connected by vias (yellow). **b** False coloured scanning electron microscopy image with included gate labelling and schematic display of later formed electron reservoirs and quantum dot positions. The CC gate will be pulsed with RF microwaves and the arrows indicate the direction of the oscillating quantum dot positions and the current path of the sensor dot. **c** Coulomb oscillations of the right qubit dot, formed below gate PR. Red dots indicate the 4 positions used to extract values for charge noise. **d** Calculated power spectral density of a 5 min timetrace taken at the indicated working point. A mean 1 Hz value of $(1.36 \pm 0.07)\ \mu eV/\sqrt{Hz}$ is extracted. The black line follows a 1/f proportionality. **e** Charge stability diagram of the two coupled qubit quantum dots, measured via charge sensing by the sensor dot. Both qubit plunger gates are swept and every visible line corresponds to a change of electron number in the respective dots, starting with a (0,0) occupation in the lower left.

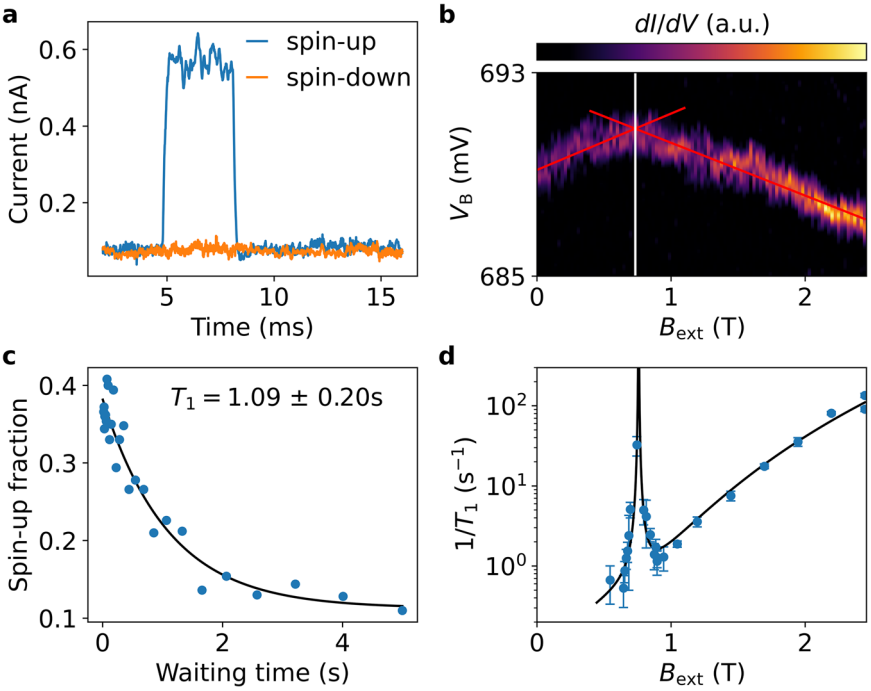

Fig. 2 | Spin relaxation time and valley splitting. **a** Measured real time SET current for a spin-up electron (blue) compared to a spin-down electron (orange). **b** Numerical derivation of the SET current tracking the 1 → 2 electron transition of the qubit dot for external magnetic fields up to 2.5 T. The barrier gate B is used as plunger gate because of the lower lever arm on the dot potential. The change in slope of the tracked transition occurs at the external field, which is equal to the two-electron singlet-triplet splitting. In the regime of strong confinement, this singlet-triplet splitting is almost equal to the valley splitting. Linear fits to the range from 0 T to 0.4 T and 1.3 T to 2.5 T result in a crossing at (0.73 ± 0.08) T which is equal to a valley splitting of (85 ± 9) μeV. **c** Elzerman pulse sequence for varying waiting times of the loading pulse at an external magnetic field of 0.66 T. The exponential decay corresponds to a spin-relaxation time $T_1 = (1.09 \pm 0.20)$ s. **d** Spin relaxation rate $1/T_1$ over external magnetic field. The black curve shows a fit combining Johnson noise and spin-phonon interaction diverging at the value corresponding to the valley splitting energy. The fit diverges at an external field of (0.76 ± 0.01) T resulting in a valley splitting of (88 ± 1) μeV.

the charge noise, we measure the power spectral density at four different working points individually. Figure 1d shows the power spectral density at the marked working point, which follows a $1/f$ proportionality often observed for charge noise in semiconducting quantum dot devices[23,24]. The mean charge noise value at 1 Hz from the four working points results to $(1.36 \pm 0.07)\ \mu eV/\sqrt{Hz}$ (for more details see Methods III B). Figure 1e shows the measured sensor current while varying both qubit plunger gate voltages. The sensor current jumps every time the electron occupation of the qubit dots changes. This charge stability diagram enables precise control of the charge state of the qubits, starting from zero electron occupation in the bottom left, up to multiple electrons in both dots in the upper right.

Spin relaxation and valley splitting

By applying an external magnetic field in x-direction, the ground state degeneracy of the electron spin state is lifted via the Zeeman effect. By tuning the quantum dot potential to an energy level between the Zeeman-split spin-down and spin-up states of the electron, a spin selective readout becomes possible. This is demonstrated in Fig. 2a, where the measured sensor current jumps between two distinct values in case of a spin-up event, or stays constant for an electron in the spin-down state. The spin relaxation time can be measured by a three stage pulse scheme[25], incorporating the spin selective readout mentioned before. In the first stage the quantum dot is emptied. In the second stage, the quantum dot potential is pulsed deep below the chemical potential of the reservoir to enable the possibility for a tunnelling electron to occupy either the ground or excited spin state. And in the third stage the quantum dot is pulsed to a level where the reservoir lies between the ground and excited spin state, to perform the spin selective readout. By varying the duration of the loading pulse, we increase the available time for a spin relaxation process to occur, which is dominated by spin-phonon interaction[26–28]. Figure 2c shows the measured spin-up fraction of 500 single shot readouts performed for different waiting times in the loading stage, at an external magnetic field of 660 mT, which is later used for qubit manipulations at resonance frequencies of ≈18.5 GHz. The spin-up fraction over waiting time is proportional to $\exp(-t/T_1)$, and the fit results in a spin relaxation time of $T_1 = (1.09 \pm 0.20)$ s.

Another important quantity for Si/SiGe heterostructures is the valley splitting energy of the two lowest valley states[27,29,30]. The conduction band minimum of silicon is normally sixfold degenerate. Straining the Si quantum well between the two SiGe layers splits the degeneracy in two energetically favourable valley states and four excited valley states. The degeneracy of the two lowest valley states gets further lifted by electrical confinement of the electron wave function, and strongly depends on sample geometry and local inhomogeneities[31,32]. To measure the valley splitting at the position of the qubit quantum dot we performed two different measurements. In Fig. 2b, the plunger gate voltage of the qubit quantum dot is varied for different total external magnetic fields. The colour axis represents the numerical derivation of the measured current through the sensor dot. The gate voltage window required for the transition from 1 to 2 electrons inside the dot is shown. The exact position of the 1 → 2 electron transition shows a change of slope at an external field strength where the Zeeman energy is equal to the two-electron singlet-triplet (ST) splitting. In the strongly confined regime, where the valley triplet has lower energy than the orbital triplet, the measured ST splitting is then nearly equal to the valley splitting[33,34]. To extract the two slopes, we fit the data in the 0 to 0.4 T interval and the 1 to 2.5 T interval separately and receive a crossing of both lines at (0.73 ± 0.08) T, which corresponds to (85 ± 9) μeV. Another method is by measuring the spin relaxation time over magnetic field. Here we observe a drastic decrease of the T_1 time, visible as a peak of the spin relaxation rate $1/T_1$, at the position where the Zeeman energy is equal to the valley splitting energy. We fit a rate equation that accounts for spin-valley mixing and intra-valley spin-orbit interaction in combination with phonon noise and Johnson noise[27,35,36]. The fit gives a peak position of (0.76 ± 0.01) T which results in a valley splitting of (88 ± 1) μeV. Both extracted values for the valley splitting are similar and correspond to a frequency above 20 GHz.

We report room-temperature Gate-to-Gate leakage tests conducted on 18 devices per die, across 13 different dies, resulting in a total of 234 tested devices with the gate architecture shown in Fig. 1b. Among these, 13 devices exhibited Gate-to-Gate leakage, resulting in a Gate yield of 94.5%. For quantum dot and qubit yields, characterisation must be performed at low temperatures. However, we currently lack a large-scale testing infrastructure for this purpose. For qubit measurements, we examined four different devices, all selected from those that did not exhibit Gate-to-Gate leakage. All four devices successfully enabled quantum dot formation and coherent spin manipulations. In the following, these four devices are labelled A to D. Device A has a CoMM gap size of 300 nm, Device B has a CoMM gap of

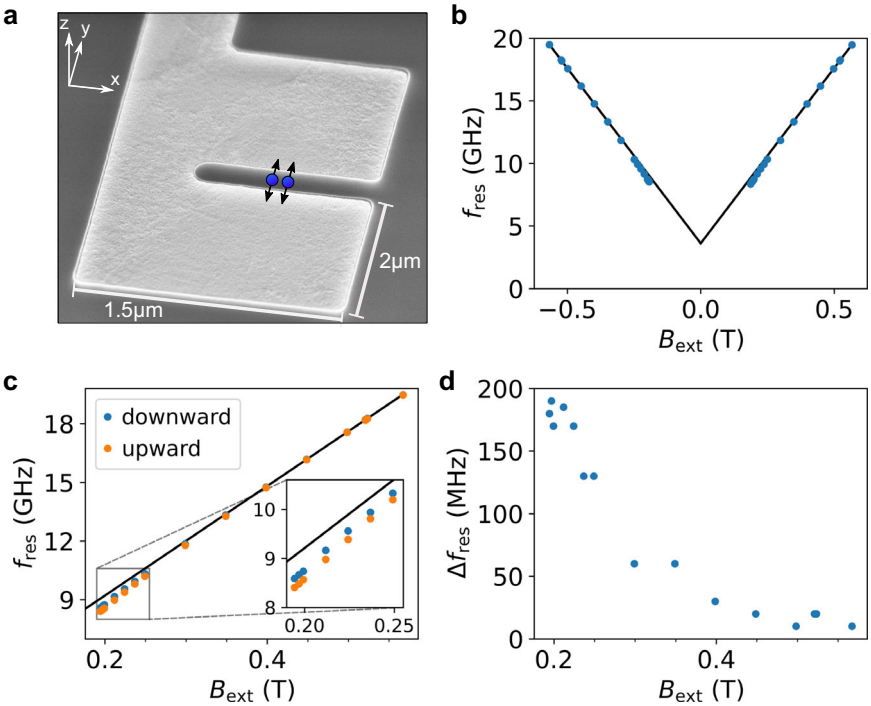

Fig. 3 | Cobalt micromagnet characterisation. **a** Scanning electron microscopy image of a cobalt micromagnet with a 300 nm gap. The image was taken from an angled viewpoint, so the lengths in the y-direction appear smaller than in the x-direction. The blue dots and black arrows indicate the position and oscillation direction of the qubit quantum dots, which are located in the quantum well ~120 nm below the CoMM. **b** Resonance frequency of the right qubit in Device A as a function of the applied external magnetic field in y-direction. The frequencies are extracted starting from the maximum external field and decreasing to zero. The two branches for positive and negative fields are measured independently. The black lines correspond to a linear fit of all resonance frequencies between 15 and 20 GHz. The contribution of the CoMM field in saturation is extracted from the y-offset of the linear fit and yields a field of (129 ± 2) mT. **c** Zoom on the positive magnetic field branch shown in (**b**), to which qubit resonance frequencies extracted from an upward magnetic field sweep have been added. The inset shows a zoom of the lowest measured resonance frequencies. **d** Difference in qubit resonance frequencies between the upward and downward sweep direction of the external magnetic field.

400 nm, and Devices C and D have CoMM gaps of 650 nm. Additionally, Devices A, B, and C originate from the same 300 mm wafer, while Device D stems from a separate wafer. In the following, all shown measurements were performed on the right qubit dot of device A (measurements of Devices B, C, and D are provided in the Supplementary Information).

Cobalt micromagnet magnetisation

Figure 3a shows a SEM image of a C-shaped CoMM with a 300 nm gap, as featured in Device A. The Co layer has a thickness of 250 nm, is encapsulated in SiO_2 and connected to a via in order to ground the micromagnet. The quantum dots are positioned in the centre of the gap ~120 nm below the CoMM. Simulations regarding the geometry and field strengths/gradients were performed in ref. 37. To characterise the behaviour of the CoMM, we measure the qubit resonance frequency for different external magnetic fields, as depicted in Fig. 3b. The resonance frequencies are extracted by first ramping the external field to its maximum value to fully saturate the CoMM and then ramping the field down to zero. The two branches corresponding to positive and negative fields are measured independently, and a linear fit of the resonance frequencies between 15 and 20 GHz yields the same y-offset of (129 ± 2) mT for both branches, which corresponds to the external field contribution in the y-direction of the CoMM in saturation.

Figure 3c shows a zoom-in on the positive magnetic field branch, to which qubit resonance frequencies from an upward magnetic field sweep have been added. For external magnetic field values below 0.3 T, the extracted resonance frequencies deviate from the linear fit. Moreover, the extracted qubit resonance frequencies vary depending on the magnetic field sweep direction and the sequence of measurements. The inset shows a zoom of the lowest measured resonance frequencies, where the deviation is greatest. We attribute this deviation to the CoMM magnetisation no longer being fully saturated, which is further evidenced by the hysteretic behaviour of the magnetisation in these magnetic field ranges. We were unable to resolve resonance frequencies below 8 GHz, a limitation we attribute to the decreasing magnetisation of the micromagnet and its field gradient, which is needed for the EDSR drive.

In Fig. 3d, the difference in qubit resonance frequencies between the upward and downward sweep directions is depicted. For external fields of 0.2 T, a resonance frequency difference of approximately 200 MHz is measured, which converges to zero for externally applied magnetic fields above 0.45 T, where the CoMM magnetisation is fully saturated.

Single qubit characterisation

For the measurements displayed in Fig. 4, every extracted spin-up fraction is the result of 200 single shot readouts. Figure 4a shows the spin-up fraction over manipulation pulse duration at qubit resonance frequency of 18.501 GHz. Typical Rabi oscillations become visible. Fitting the oscillations gives a Rabi frequency of 5.2 MHz for an applied RF microwave power of 24 dBm. Figure 4b displays the spin up fractions for different microwave source output powers in dBm over pulse duration, and Fig. 4c shows the extracted Rabi frequency for the respective microwave amplitudes (10 to 23 dBm subtracted by 45 dB inline attenuation and converted to mV). The Rabi frequencies follow a clear linear behaviour over increasing microwave amplitude up to values above ≈14 mV, where a saturation starts to set in. The black line corresponds to a linear fit of the data excluding the resulting Rabi frequencies for the 5 highest amplitudes. Saturation is a sign of a different qubit drive regime, which could be caused by either a lower magnetic field gradient for higher RF amplitudes or a strong quantum dot confinement in the x-direction, dampening larger displacements of the quantum dot position. Figure 4d shows a Ramsey measurement where the waiting time τ between two $\pi/2$ pulses is varied. A fixed detuning of 2 MHz creates an additional z-rotation on the Bloch sphere during the waiting time τ at that frequency. Fitting the oscillations with a sine multiplied by a $\exp(-(t/T_2^*)^2)$ term gives a coherence time $T_2^* = (1.05 \pm 0.08)\,\mu s$, similar to the reported values in other natural silicon spin qubit devices[38] and consistent for all four measured qubit devices in this work (see Supplementary Information). Figure 4e displays the results for a Hahn echo experiment, fitted with $\exp(-(t/T_2^H)^\alpha)$. The extracted T_2^H equals $(51.24 \pm 1.49)\,\mu s$ with an exponent $\alpha = 2.06 \pm 0.17$ corresponding to a gaussian damped exponential decay, observed in systems where the dominant decoherence mechanism follows a $1/f$ frequency dependence[23,39,40]. The comparison between T_2^* and T_2^H shows the frequency dependence of the dominant decoherence channel, indicating that the noise amplitudes increase to lower frequencies. Considering the abundance of nuclear spins of ^{29}Si isotopes in natural silicon, it was demonstrated that

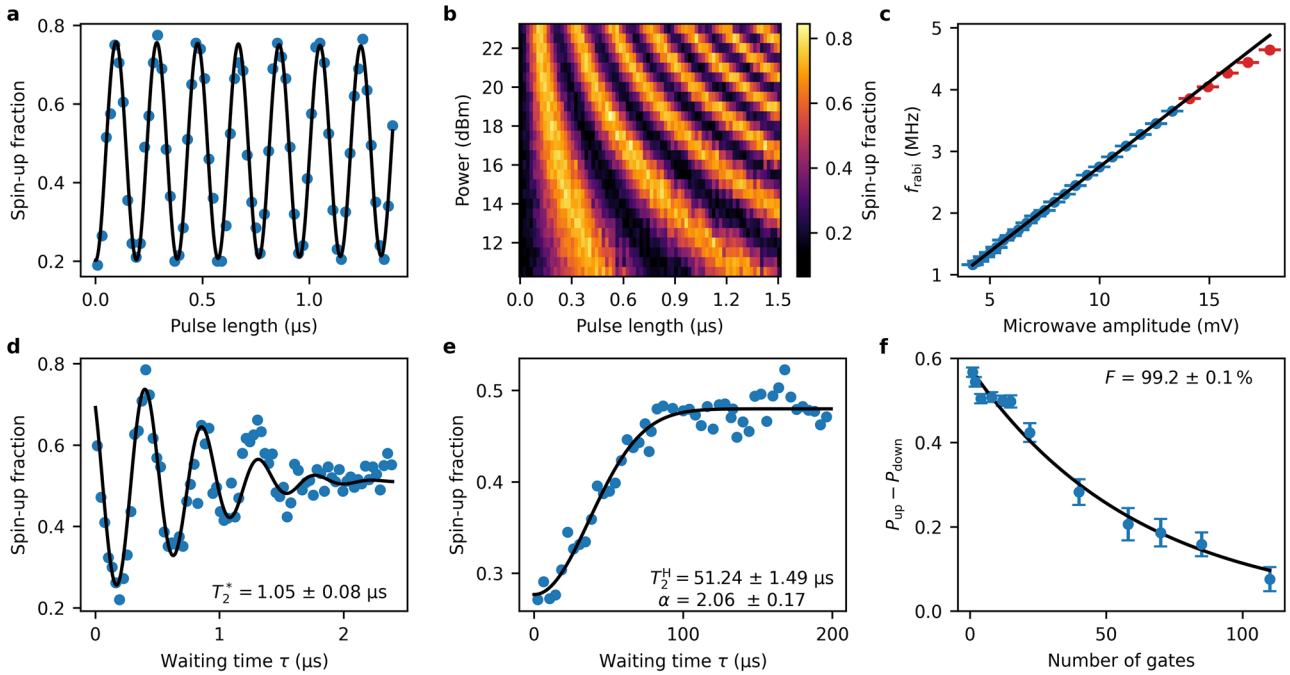

Fig. 4 | Qubit characterisation of the right qubit in device A. a Rabi measurement on resonance with 24 dBm output power up to a pulse length of 1.5 μs. A Rabi frequency of 5.2 MHz is extracted by fitting a sine function to the data. No dampening of the frequency amplitude is visible up to this pulse length. **b** Same measurement as in **a** for varying RF output powers. **c** Extracted Rabi frequencies for all used powers of the measurement shown in **b** over the applied power converted to the correspinding microwave amplitude in mV. The black line corresponds to a linear fit excluding the 5 data points of highest applied power (marked in red). **d** Ramsey measurement for a fixed detuning of 2 MHz. The black curve corresponds to a gaussian damped sine and gives a T_2^* value of (1.05 ± 0.08) μs. **e** Spin-echo measurement fitted with $\exp(-(t/T_2^H)^\alpha)$, yielding $T_2^H = (51.2 \pm 1.5)$ μs with $\alpha = 2.06 \pm 0.17$. **f** Difference of spin-up and spin-down fraction depending on the length of a randomised gate sequence. The black curve corresponds to a fit of the form $A \cdot P^n$ which yields the primitive gate fidelity $F = 1 - (1 - P)/2 = (99.2 \pm 0.1)\%$.

fluctuating nuclear spins in the vicinity of the qubit are the dominant decoherence mechanism[4,30]. Isotopic enrichment of ^{28}Si can therefore drastically reduce this low-frequency decoherence channel and thus increase the T_2^* time by orders of magnitude[12,20,41]. To measure the single qubit gate fidelity, we performed randomised benchmarking experiments. For this, starting from a defined initial state, a random sequence of n Clifford gates is performed. A final gate ideally brings the qubit back to a desired final state for readout. With increasing n the probability to reach this desired final state will decrease due to gate errors, and finite qubit lifetimes. By fitting the deviation of the ideal final state over the length n of the random sequence, we can extract the single qubit gate fidelity. To increase the robustness to readout working point deviations, we perform each random gate sequence with a final projection into the spin-up state and a final projection into the spin-down state, and subtract the resulting spin-up probabilities from each other to obtain the difference $P_{up} - P_{down}$ between the two final states. This difference starts at a maximum value for a small n and converges to zero for large n, where the quantum information is completely lost. In the experiment the primitive gate set $\{I, \pm X, \pm Y, \pm X^2, \pm Y^2\}$ is used to construct all 24 single qubit Clifford gates, where a Clifford gate consists in average of 1.875 primitive gates (for details see supplemental materials). Figure 4f shows the result of the performed randomised benchmarking. Each measured $P_{up} - P_{down}$ value is the result of 40 randomised gate sequences of length n and is fitted with $A \cdot P^n$ from which we extract the gate fidelity $F = 1 - (1 - P)/2$. For the primitive gate fidelity, we extract a value of (99.2 ± 0.1)% which converts to a Clifford gate fidelity of (98.5 ± 0.1)%.

In conclusion, we demonstrate the formation and operation of EDSR qubits in natural Si/SiGe heterostructures fully fabricated and grown in a 300 mm industrial semiconducting wafer process line. We report a charge noise value of $(1.36 \pm 0.07)\ \mu eV/\sqrt{Hz}$ and valley splitting energies above 84 μeV. We achieve spin relaxation times T_1 above 1 s and coherence times T_2^* and T_2^H of 1 μs and 50 μs respectively. Paired with Rabi frequencies up to 5 MHz we achieve single qubit gate fidelities of 99.2%. Fluctuating nuclear spins of ^{29}Si isotopes in natural silicon are known to limit qubit lifetimes especially in the low frequency regime, and isotopic purification of ^{28}Si in the quantum well is expected to enhance especially the T_2^* time by at least one order of magnitude. In addition, optimisation of the material, geometry and position of the micromagnet could further increase the manipulation speed of the qubit and improve gate fidelity. Overall, these results demonstrate the operation of state of the art spin qubit devices following industrial 300 mm wafer process design rules. This opens the door for the optimisation of qubit metrics on a large scale and the development of much larger and more complex spin qubit architectures required for the realisation of a universal quantum computer.

Methods

Measurement setup

The samples were cooled in a Qinu Version XL dilution refrigerator, with an operating temperature of about 30 mK. The DC lines are filtered by two RC low pass filter stages at mK with cutoff frequencies of 250 Hz for the static gate voltages, and 40 kHz for DC lines used for current measurements through the charge sensor and qubit plunger voltage pulses. Additionally, every line was filtered by a LFCN-80+ for mid range frequency filtering between 225 MHz and 4500 MHz. An electron temperature of 120 mK is extracted from the width of the 0 → 1 qubit charge transition. RF pulses are sent through CuNi coaxial cables with 26 dB attenuation at 18.5 GHz at room temperature, and an additional 19 dB inline attenuation. The RF signal is capacitively coupled to the DC line on the printed circuit board which is wire bonded to the central screening gate (CC) of the sample. All static voltages were applied by an Adwin Pro II from Jaeger Messtechnik. The measured current through the sensor dot was converted to a voltage at room temperature by an SP983c Basel Precision Instruments I–V converter, and the voltage was digitised by an analogue input module of the Adwin Pro II. Qubit plunger voltage pulses were realised with an

HDAWG from Zurich Instruments. EDSR microwave manipulation was done by controlling the in-phase (I) and quadrature (Q) channels of an SMW200A Rohde & Schwarz vector signal generator by two HDAWG outputs.

Charge noise measurements

The 1 Hz charge noise value for a certain working point is extracted by taking a 5 min long timetrace of the current data. The timetrace is converted to a power spectral density using the Welch method. Welch's method[42] computes the power spectral density by dividing the timetrace into overlapping segments and averaging them. Additionally, a window function is applied to the individual segments. The use of the window function averages noise in the estimated power spectrum in exchange for a reduced frequency resolution because of overlapping time windows. A Hann function was used as the window function. The resulting power spectral density is then normalised with the slope of the Coulomb oscillation at the used working point and converted to eV by multiplying with the plunger gate lever arm. The lever arm for gate PR was derived from Coulomb diamond measurements in which the source-drain bias voltage is varied over changing plunger gate voltages. By determining the slope of the diamond edges close to the zero source-drain bias range, in order to minimise the effect of higher-order tunnelling contributions, we extract a lever arm of (0.10 ± 0.01) eV/V. The final power spectral density is then fitted with a a/f^b function and the value for 1 Hz is extracted.

Single shot spin selective readout

In order to differentiate between the spin-up and spin-down state of a tunnelling electron, we tune the plunger gate voltage of the qubit dot so that the Fermi energy of the reservoir lies between the Zeeman-split ground state energies of the electron in the qubit quantum dot. The tunnelling rate between qubit dot and reservoir is tuned to ≈1 kHz and the standard readout time window used for the single shot measurements is 15 ms. Depending on the sign of the current jump caused by a tunnelling electron, the entire trace is multiplied by −1 to ensure that the change on the SET current is always positive. The measured current is then subtracted by the baseline current. Each sample is digitised into either 0 or 1 by a fixed current threshold, where 1 corresponds to the time in which no electron occupies the qubit dot, while at 0 the dot is occupied by an electron. If a trace contains even a single digital 1, it will be counted as a spin-up event, independent of the number of jumps inside a single trace, so multiple current jumps inside a single readout window due to e.g. thermal excitation, will be counted the same as a single current jump. The resulting spin-up fraction is then calculated by dividing the number of traces containing a digital one by the total number of traces.

Data availability

The datasets generated and/or analysed during this study are available from the corresponding authors on reasonable request.

Data availability

The datasets generated and/or analysed during this study are available from the corresponding authors on reasonable request.

Received: 20 September 2024; Accepted: 23 March 2025;
Published online: 05 April 2025

References

1. Loss, D. & DiVincenzo, D. P. Quantum computation with quantum dots. *Phys. Rev. A* **57**, 120 (1998).
2. Vandersypen, L. M. K. et al. Interfacing spin qubits in quantum dots and donors–hot, dense, and coherent. *npj Quantum Inf.* **3**, 34 (2017).
3. Yoneda, J. et al. A quantum-dot spin qubit with coherence limited by charge noise and fidelity higher than 99.9%. *Nat. Nanotechnol.* **13**, 102 (2018).
4. Xue, X. et al. Benchmarking Gate Fidelities in a Si / SiGe Two-Qubit Device. *Phys. Rev. X* **9**, 021011 (2019).
5. Huang, W. et al. Fidelity benchmarks for two-qubit gates in silicon. *Nature* **569**, 532 (2019).
6. Ono, K., Mori, T. & Moriyama, S. High-temperature operation of a silicon qubit. *Sci. Rep.* **9**, 469 (2019).
7. Undseth, B. et al. Hotter is easier: unexpected temperature dependence of spin qubit frequencies. *Phys. Rev. X* **13**, 041015 (2023).
8. Huang, J. Y. et al. High-fidelity spin qubit operation and algorithmic initialization above 1 K. *Nature* **627**, 772 (2024).
9. Seidler, I. et al. Conveyor-mode single-electron shuttling in Si/SiGe for a scalable quantum computing architecture. *npj Quantum Inf.* **8**, 100 (2022).
10. Dijkema, J. et al. Cavity-mediated iSWAP oscillations between distant spins. *Nat. Phys*. **21**, 168–174 (2025).
11. De Smet, M. et al. High-fidelity single-spin shuttling in silicon (2024), arXiv:2406.07267 [cond-mat, physics:quant-ph].
12. Philips, S. G. J. et al. Universal control of a six-qubit quantum processor in silicon. *Nature* **609**, 919 (2022).
13. Shehata, M. M. E. K. et al. Modeling semiconductor spin qubits and their charge noise environment for quantum gate fidelity estimation. *Phys. Rev. B* **108**, 045305 (2023).
14. Fleetwood, D. M. et al. Effects of oxide traps, interface traps, and "border traps" on metal-oxide-semiconductor devices. *J. Appl. Phys.* **73**, 5058 (1993).
15. Dutta, P. & Horn, P. M. Low-frequency fluctuations in solids: 1 f noise. *Rev. Mod. Phys.* **53**, 497 (1981).
16. Rocki, K. et al. Fast Stencil-Code Computation on a Wafer-Scale Processor (2020), arXiv:2010.03660 [cs].
17. Maurand, R. et al. A CMOS silicon spin qubit. *Nat. Commun.* **7**, 13575 (2016).
18. Zwerver, A. M. J. et al. Qubits made by advanced semiconductor manufacturing. *Nat. Electron.* **5**, 184 (2022).
19. Klemt, B. et al. Electrical manipulation of a single electron spin in CMOS using a micromagnet and spin-valley coupling. *npj Quantum Inf.* **9**, 107 (2023).
20. Neyens, S. et al. Probing single electrons across 300-mm spin qubit wafers. *Nature* **629**, 80 (2024).
21. Elsayed, A. et al. Low charge noise quantum dots with industrial CMOS manufacturing. *npj Quantum Inf.* **10**, 70 (2024).
22. Pioro-Ladrière, M. et al. Electrically driven single-electron spin resonance in a slanting Zeeman field. *Nat. Phys.* **4**, 776 (2008).
23. Paladino, E., Galperin, Y., Falci, G. & Altshuler, B. 1 / f noise: Implications for solid-state quantum information. *Rev. Mod. Phys.* **86**, 361 (2014).
24. Ferrero, J. et al. Noise reduction by bias cooling in gated si/sige quantum dots. *Appl. Phys. Lett.* **124**, 204002 (2024).
25. Elzerman, J. M. et al. Single-shot read-out of an individual electron spin in a quantum dot. *Nature* **430**, 431 (2004).
26. Huang, P. & Hu, X. Spin relaxation in a Si quantum dot due to spin-valley mixing. *Phys. Rev. B* **90**, 235315 (2014).
27. Hollmann, A. et al. Large, tunable valley splitting and single-spin relaxation mechanisms in a Si / Si Ge Quantum Dot. *Phys. Rev. Appl.* **13**, 034068 (2020).
28. Borjans, F., Zajac, D., Hazard, T. & Petta, J. Single-spin relaxation in a synthetic spin-orbit field. *Phys. Rev. Appl.* **11**, 044063 (2019).
29. Burkard, G., Ladd, T. D., Pan, A., Nichol, J. M. & Petta, J. R. Semiconductor spin qubits. *Rev. Mod. Phys.* **95**, 025003 (2023).
30. Zwanenburg, F. A. et al. Silicon quantum electronics. *Rev. Mod. Phys.* **85**, 961 (2013).
31. Hosseinkhani, A. & Burkard, G. Electromagnetic control of valley splitting in ideal and disordered Si quantum dots. *Phys. Rev. Res.* **2**, 043180 (2020).
32. Volmer, M. et al. Mapping of valley splitting by conveyor-mode spin-coherent electron shuttling. *npj Quantum Inf.* **10**, 61 (2024).

33. Ercan, H. E., Coppersmith, S. N. & Friesen, M. Strong electron-electron interactions in si/sige quantum dots. *Phys. Rev. B* **104**, 235302 (2021).
34. Dodson, J. P. et al. How valley-orbit states in silicon quantum dots probe quantum well interfaces. *Phys. Rev. Lett.* **128**, 146802 (2022).
35. Yang, C. H. et al. Spin-valley lifetimes in a silicon quantum dot with tunable valley splitting. *Nat. Commun.* **4**, 2069 (2013).
36. Petit, L. et al. Spin lifetime and charge noise in hot silicon quantum dot qubits. *Phys. Rev. Lett.* **121**, 076801 (2018).
37. Dumoulin Stuyck, N. I. et al. Low dephasing and robust micromagnet designs for silicon spin qubits. *Appl. Phys. Lett.* **119**, 094001 (2021).
38. Stano, P. & Loss, D. Review of performance metrics of spin qubits in gated semiconducting nanostructures. *Nat. Rev. Phys.* **4**, 672 (2022).
39. Hanson, R., Kouwenhoven, L. P., Petta, J. R., Tarucha, S. & Vandersypen, L. M. K. Spins in few-electron quantum dots. *Rev. Mod. Phys.* **79**, 1217 (2007).
40. McCourt, T. et al. Learning noise via dynamical decoupling of entangled qubits. *Phys. Rev. A* **107**, 052610 (2023).
41. Muhonen, J. T. et al. Storing quantum information for 30 seconds in a nanoelectronic device. *Nat. Nanotechnol.* **9**, 986 (2014).
42. Welch, P. The use of fast Fourier transform for the estimation of power spectra: A method based on time averaging over short, modified periodograms. *IEEE Trans. Audio Electroacoustics* **15**, 70 (1967).

Acknowledgements

We thank C. Sürgers for general advice and help with the measurement electronics and T. Cubaynes for the design of the sample printed circuit board. We further thank the German Research Foundation (DFG) for the Gottfried Wilhelm Leibniz-Award, ZVN-2020 WE 4458-5 for financial support. The work at imec was supported by the imec Industrial Affiliation Program on Quantum Computing, and the European Union's Horizon 2020 Research and Innovation Programme under grant agreement No 951852 (QLSI).

Author contributions

T.K. conducted the experiments and performed data analysis. R.L. grew the heterostructure. S.K. and S.M. fabricated the devices, R.L. and C.G. designed and shared the devices. G.S. made micromagnet simulations. J.F. developed the measurement software. T.K., C.G., V.A., D.S., and N.G. collaboratively discussed and interpreted the results. T.K. and C.G. drafted the manuscript, with input and feedback from all co-authors. D.W., K.D.G., and W.W. supervised and coordinated the project.

Funding

Open Access funding enabled and organized by Projekt DEAL.

Data availability

The datasets generated and/or analysed during this study are available from the corresponding authors on reasonable request.

Competing interests

The authors declare no competing interests.

Additional information

Supplementary information The online version contains supplementary material available at https://doi.org/10.1038/s41534-025-01016-x.

Correspondence and requests for materials should be addressed to Thomas Koch or Wolfgang Wernsdorfer.